Invited Paper

Carbon-based Nano-electro-mechanical-systems

A. B. Kaul[(a)], A. R. Khan, K. G. Megerian, L. Epp, H. G. LeDuc, and L. Bagge
Jet Propulsion Laboratory, California Institute of Technology, Pasadena, CA 91109

A. T. Jennings, D. Jang, and J. R. Greer
Division of Engineering and Applied Science, California Institute of Technology, Pasadena, CA 91125

ABSTRACT

We provide an overview of our work where carbon-based nanostructures have been applied to two-dimensional (2D) planar and three-dimensional (3D) vertically-oriented nano-electro-mechanical (NEM) switches. In the first configuration, laterally oriented single-walled nanotubes (SWNTs) synthesized using thermal chemical vapor deposition (CVD) were implemented for forming bridge-type 2D NEMS switches, where switching voltages were on the order of a few volts. In the second configuration, vertically oriented carbon nanofibers (CNFs) synthesized using plasma-enhanced (PE) CVD have been explored for their potential application in 3D NEMS. We have performed nanomechanical measurements on such vertically oriented tubes using nanoindentation to determine the mechanical properties of the CNFs. Electrostatic switching was demonstrated in the CNFs synthesized on refractory metallic nitride substrates, where a nanoprobe was used as the actuating electrode inside a scanning-electron-microscope. The switching voltages were determined to be in the tens of volts range and van der Waals interactions at these length scales appeared significant, suggesting such structures are promising for nonvolatile memory applications. A finite element model was also developed to determine a theoretical pull-in voltage which was compared to experimental results.

1. INTRODUCTION

The Complementary-Metal-Oxide-Semiconductor (CMOS) industry faces major obstacles to further miniaturization beyond the 22 nm integrated-circuit (IC) lithography node. Carbon nanotubes (CNTs) and carbon nanofibers (CNFs) are among the materials being considered as viable candidates for overcoming some of the issues that arise from the downscaling of IC dimensions, which include electromigration encountered with Copper (Cu) interconnects, or high leakage currents that arise from gate dielectrics just a few nanometers (nm) in thickness. While CNTs are showing promise as interconnects due to their high current carrying ability,[1] as well as efficient heat transporting assemblies,[2] another area that is receiving intense interest is the application of CNTs in nano-electro-mechanical-systems (NEMS), as indicated by the International Technology Roadmap for Semiconductors (ITRS).[3] The physical isolation of conducting paths

[(a)]Email: anupama.b.kaul@jpl.nasa.gov

Micro- and Nanotechnology Sensors, Systems, and Applications II,
edited by Thomas George, M. Saif Islam, Achyut K. Dutta, Proc. of SPIE Vol. 7679,
76790N · © 2010 SPIE · CCC code: 0277-786X/10/$18 · doi: 10.1117/12.851293

in NEMS reduces leakage currents and power dissipation, which are parameters difficult to constrain with increasingly miniaturized Si transistors with their short source-drain channel lengths or ultra-thin gate oxides. In addition, Si reverts to intrinsic behavior at low- and high-temperatures due to Fermi level shifting, which makes solid-state transistors in general more susceptible to thermal extremes. The underlying mechanical operation of NEMS structures is also suggestive of their inherent tolerance toward harsh thermal, as well as high radiation environments, which potentially enhances their ruggedness over solid-state transistors.

In particular, carbon based nanostructures offer advantages due to their exceptional elasticity compared to inorganic nanowires[4] for example, for extending their mechanical cycling longevity for NEMS applications. Such exceptional mechanical properties arise from the sp^2 bonding character inherent to graphene from which many carbon-based nanostructures are derived, such as single-walled nanotubes (SWNTs), multi-walled nanotubes (MWNTs) or CNFs. The success of CNT based NEMS has already been validated in a variety of applications ranging from nanotweezers,[5] memory devices,[6] nanorelays,[7,8] and resonators.[9] In this paper, we provide an overview of our work in forming NEMS switches which are comprised of laterally oriented SWNTs suspended over pre-fabricated trenches based on two-dimensional (2D) planar technology, as well as vertically oriented CNFs which are under consideration for three-dimensional (3D) NEMS.

2. NEMS Switch Topologies

For the 2D planar applications of CNTs for NEMS, the two primary configurations that have typically been explored rely on the bridge or cantilever geometries, as illustrated in Fig. 1a. In our work, we have formed 2D bridge-based NEMS switches from SWNTs, where the tubes lie above a refractory metal layer which is used for actuating the SWNT. This work is described in more detail in Section 3.1. An alternative geometry also exists that's comprised of vertically oriented tubes for 3D NEMS, which we are also presently exploring. A schematic of such a configuration is depicted in Fig. 1b, where a single, vertically-oriented tube is seen before and during electrostatic actuation, which is a 3D NEMS architecture that has the potential to increase integration densities by at least 1 or 2 orders of magnitude compared to 2D planar NEMS geometries.

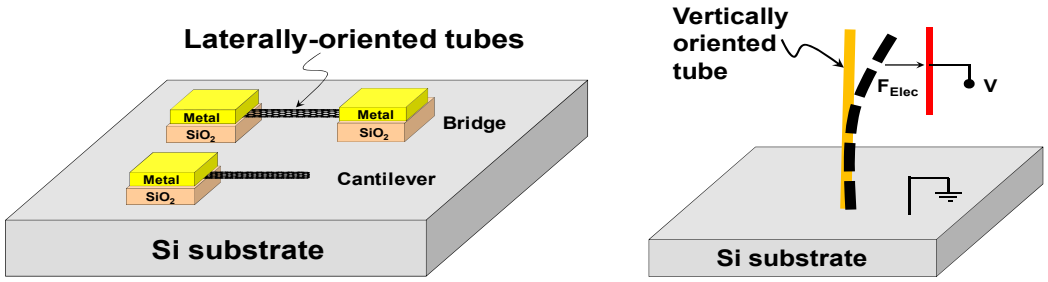

(a) (b)

Figure 1. (a) The bridge or cantilever configurations is characteristic of 2D planar applications of laterally oriented tubes, which was one of the topologies explored here for our SWNT-based 2D NEMS switches. (b) A schematic showing a single, vertically oriented CNF, where an electrostatic force F_{elec} arises when a voltage V is applied on a nanoprobe in close proximity to the tube, causing the CNF to bend. The mechanical robustness of the CNFs, as well as their electrical properties, were measured and are reported here to determine the suitability of such bottom-up synthesized structures for 3D NEMS. Not to scale.

By applying a voltage V on a nanoprobe in close proximity to a single tube, as shown in Fig. 1b, an electrostatic force F_{elec} is generated which deflects the tube to the right. Jang *et al.* have recently demonstrated electrostatic switching between vertically oriented CNFs arranged in a 3-terminal configuration.[10,11] In addition, Hayanmizu *et al.* have implemented lithographically fabricated 2D CNT

assemblies and integrated such structures in a 3D framework.[12] Recently, *in-situ* techniques were also used to characterize the electrical performance of Germanium (Ge) nanowires[13] and MWNTs[14] that were physically welded or connected to the ends of metallic probe tips for NEMS applications. In our work on 3D NEMS, we have examined the nanomechanical properties of the tubes using *in situ* techniques which are described in Section 3.2. We have also performed electrical actuation measurements on such tubes and these results are described in Section 3.3. Finally, finite element modeling (FEM) results are also described and reported in Section 3.4, where the measured pull-in voltages V_{pi} are compared to those obtained from simulation.

3. RESULTS AND DISCUSSION

3.1 Lateral NEMS Switches

The SWNTs which are the actuating elements in our laterally-oriented 2D NEMS switches were formed using thermal chemical vapor deposition (CVD) with iron (Fe) catalyst using procedures described in more detail elsewhere.[15] An SEM micrograph of a finished device is shown in Fig. 2a, which depicts a SWNT crossing the trench with the Nb pull electrode directly beneath the tube. The actuation voltages were measured by applying a dc voltage between the left (or right electrode) and the pull electrode. As transient charge develops on the tube with increasing bias voltage, the resulting electrostatic force is sufficient to overcome the elastostatic force and deflects the suspended tube down toward the pull electrode underneath. The current was measured as a function of the dc bias voltage between the left (or right) electrode and the pull electrodes.

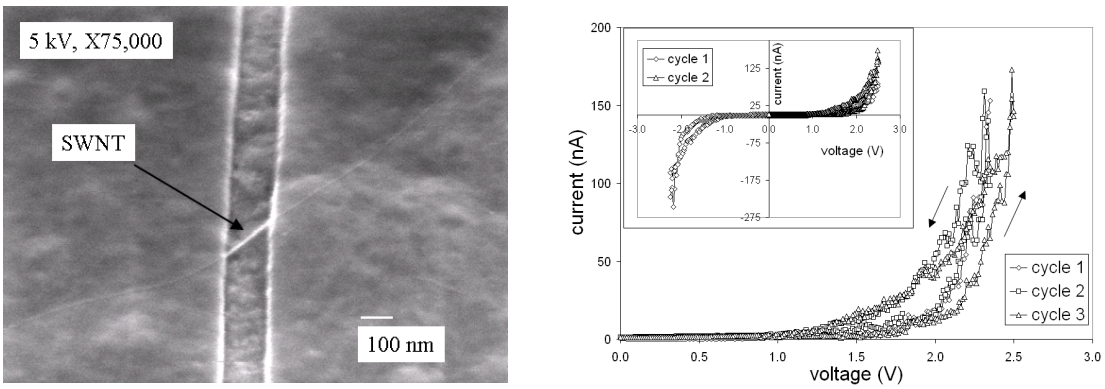

(a) (b)

Figure 2. (a) High magnification SEM micrograph shows a single nanotube bridging the 130 nm wide trench. (b) I-V characteristic of a device actuated over multiple cycles (250 nm trench width). The inset shows the ON state voltage to be similar in the forward-bias (pull electrode grounded) and reverse-bias (pull electrode positive) regimes, indicating that field emission is an unlikely possibility at these voltages.

Shown in Fig. 2b is an I-V characteristic of a device that was actuated over several cycles. Turn-on occurs at ~ 2.4 V in this case, with a slight variation with cycling that is also reported in other CNT and MEMS switches. The rapidly rising current regime arises in both the forward-biased (pull electrode grounded) and reverse-biased (pull electrode positive) cases, as indicated by the inset of Fig. 2b, although the exact switching voltages are slightly different in the two cases, ~ 2.4 V (forward-biased) and ~ 2.2 V (reverse-biased). The differences in turn-on voltage can perhaps arise from the random distribution of metallic and semiconducting tubes observed in current SWNT growth processes, but still suggest that the differences in

resistance between the ON and OFF states far outweigh any differences that may arise from contact resistances. As shown by the inset of Fig. 2b, this switching behavior is polarity independent, as would be expected for electrostatic actuation, and rules out field emission as a likely mechanism at these voltages. This switching between the low- and high-current states represents more than a ~ 4 order of magnitude increase, implying well-defined OFF and ON states, respectively. In the rapidly rising current regime, the data is increasingly noisy, reflecting the stochastic nature of the tunneling mechanism. Hysteresis between the increasing and decreasing bias voltage paths was also evident, as illustrated in Fig. 2b, and arises from the interaction of the tube with surface van der Waals forces. Lateral leakage currents within the dielectric were extremely small, ~ 10 pA at +/- 5 V.

In general, the magnitude of the switching voltages in these air-bridge SWNT-based NEMS switches was a few volts, which is smaller by at least an order of magnitude compared to actuation voltages typically observed in MEMS switches.[16] In cantilever CNT devices,[17] the turn-on voltages were also somewhat higher in the 6 – 20 V range. The differences in device geometries, such as larger air-gaps (~ 80 nm) and the use of MWNTs may be sufficient to explain the larger turn-on voltages required in that case. However, Dujardin[7] *et al.* report low switching voltages of 2.8 V – 3.0 V in their MWNTs cantilever structures, a result which can be attributed to the very shallow (4 nm) air gaps. We have also measured the switching times to be on the order of a few nanoseconds on these switches,[15] which is extremely attractive for high-frequency electronics applications.

3.2 In-Situ Nanomechanical Measurements

In order to increase integration densities further, we have also explored the use of vertically oriented CNFs for 3D NEMS applications which is now discussed in more detail here. In this section, we examine the nanomechanical properties of the *as-grown* CNFs which are monolithically integrated on Si substrates, in order to determine the suitability of such bottom-up structures for 3D NEMS applications. As the CNF bends from the application of an electrostatic force (Fig. 1b), it induces mechanical strains along its height, which generates stress concentrators at several locations, for example, at the CNF-to-substrate interface, as well as within the body. The CNFs need to withstand such stresses since it directly impacts their cycling longevity for NEMS applications. Nanomechanical measurements were conducted to decipher the mechanical robustness of the CNFs through nanoindentation and uniaxial compression tests made with a custom-built *in-situ* nanomechanical testing instrument, SEMentor.[18] A Berkovich tip, which is a pyramidal, shallow-angled tip, was used to indent a forest of CNFs, as shown in Fig. 3a. The SEM image taken after indentation (Fig. 3b) revealed that the CNFs fractured at the base, with the fracture angle α_f of ~ 25º- 35º (relative to the CNF or central axis).

The significance of α_f was correlated to the structural characteristics of the CNFs that was obtained via Transmission Electron Microscopy (TEM) analysis. Microstructural analysis was performed in the FEI Tecnai-F20 Scanning- (S) TEM, with a field emission source of 200 kV. Analysis of the mechanically transferred CNFs grown directly on Si revealed a structure where the graphite basal planes were inclined to the central axis (Fig. 3c) at a cone angle denoted by α (Fig. 3d). This so-called herring-bone structure is commonly observed with PECVD synthesized CNFs,[19] and for our particular CNFs α was determined to be ~ 30º (Fig. 3d), but it can increase as the hydrogen content during growth is increased. It is interesting to note that α_f and α do not differ from each other appreciably, suggesting that the CNFs sheared within the basal planes which are held by the relatively weak van der Waals forces, and the CNF-to-substrate adhesion is relatively strong.

We also conducted *in-situ* uniaxial compression tests on single CNFs to evaluate their axial Young's modulus, *E*. Prior reports on uniaxial compression tests performed by Waters *et al.* were conducted on arrays of MWCNTs,[20] and Qi *et al.* used a nanoindentor, in conjunction with statistical approaches, to characterize forests of vertically aligned CNFs.[21] More recently, Hayamizu *et al.* have determined the mechanical properties of lithographically fabricated beams composed of self-assembled SWCNT arrays that were excited photothermally into resonance.[22] The SEM image in Fig. 4a shows a CNF just prior to compressive loading,

where the load was applied with a flat punch indenter tip rather than with a Berkovich tip. From the force-deflection plot shown in Fig. 4b, the maximum applied axial force F_z that the tube was able to sustain before buckling was determined to be ~ 6.4 μN. The initial length of the tube L_o shown in Fig. 4a was ~ 1.75 μm, and due to its tapered profile, the top and bottom tube diameters were measured to be ~ 40 nm and ~ 90 nm, respectively. From this, the modulus E was calculated using $E = \frac{F_z L_o}{\pi r_b r_t (L_o - u_z)}$, where u_z is the height of the tube prior to buckling, and r_b and r_t are the tube diameters at the bottom and top, respectively. With these parameters, E was calculated to be ~ 816 GPa, which appears to be comparable to the value obtained by Qi *et al.* for measurements conducted on arrays of vertically aligned CNFs, where an axial E as low as 900 GPa was deciphered.[21] This difference is likely a result of the assumption of structural homogeneity within the tube.

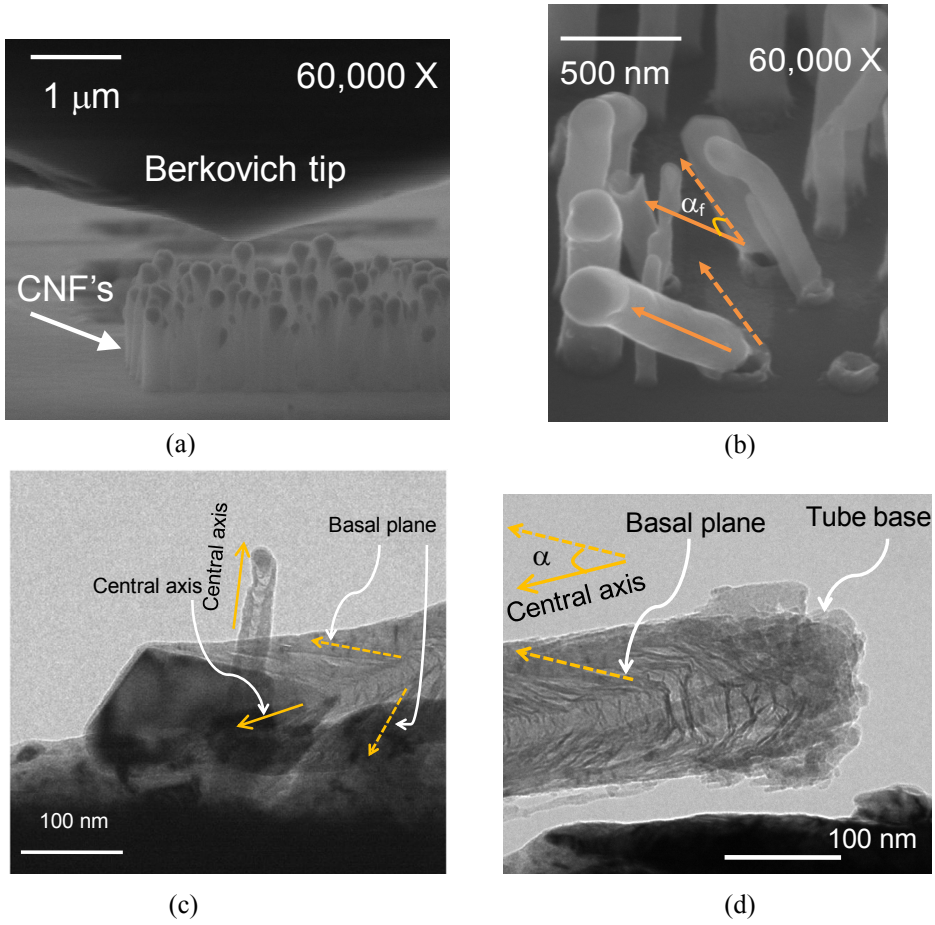

Figure 3. (a) A Berkovich tip was used to mechanically bend a forest of CNFs in a SEMentor Image is taken before deformation. (b) An SEM image of the CNFs taken after the mechanical bending tests, which indicated the CNFs fracture at an angle α_f ~ 25º-35º relative to the fiber axis (solid line). (c) TEM image of two CNFs indicating the direction of the graphite basal planes (dotted line) α relative to the central axis (solid line). (d) A cone angle α ~ 30º was determined for this CNF, which did not differ appreciably from α_f. This suggests the CNFs sheared from the basal planes in (b) and that the CNF-to-substrate adhesion is strong.

The SEM image in Fig. 4c depicts the same tube after the test and shows that it has buckled plastically, as expected for a column whose length exceeds the shell buckling criteria (50-100 nm long CNFs).[23] The uniaxial compression tests performed here suggest an Euler-type column buckling, which has also been observed by Fukuda *et al.* for measurements performed on MWCNTs with their predominantly hollow structure.[24] Our measurements demonstrate the remarkable ability of the CNF to recover post-deformation, which should be beneficial to enhancing their robustness for NEMS applications. In addition, the relatively large magnitude of E in comparison with Si (E ~ 165 GPa), a commonly used material for micro-electro-mechanical-systems (MEMS), renders CNFs to be lucrative candidates for high-speed NEMS.

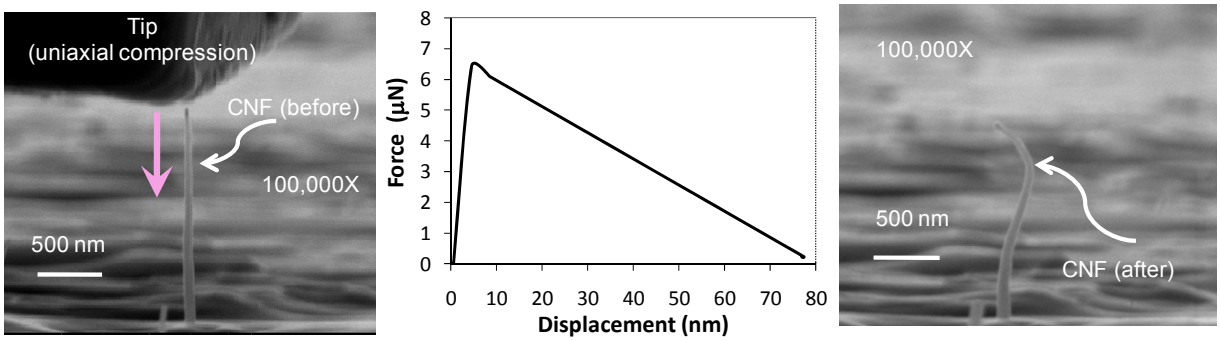

(a) (b) (c)

Figure 4. (a) A single CNF with L_o ~ 1.75 μm in close proximity to a flat punch indenter tip which was used to load the CNF in uniaxial compression. (b) The corresponding force-displacement characteristic for the tube in (a) as it was compressed from which E ~ 816 GPa was computed. (c) The tube in (a) after the compression test, indicating plastic buckling.

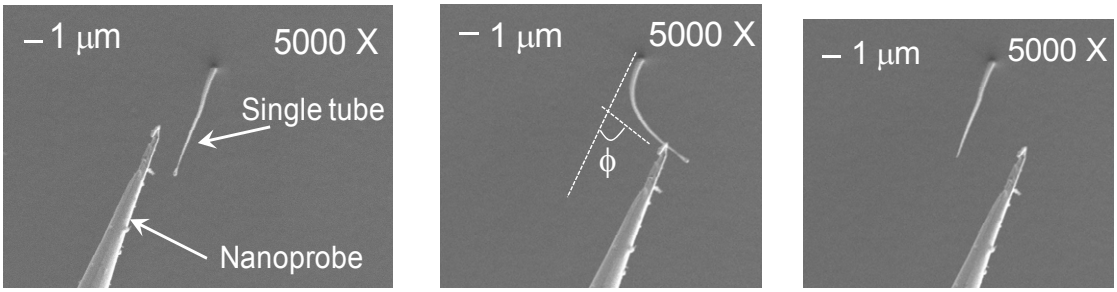

(a) (b) (c)

Figure 5. (a) A nanoprobe was in close proximity to a single CNF. (b) The probe was mechanically manipulated so that it deflected the CNF to the right. The CNF accommodated large bending angle without fracture or delamination, with ϕ ~ 70º over tens of cycles. (c) The CNF returned elastically to its initial position after the probe was removed. Such measurements suggest that the CNFs are mechanically resilient, and should enable enhanced cycling longevity for NEMS applications.

Bending tests were also conducted on individual CNFs using a nanoprobe inside an SEM, as shown in Fig. 5a. The nanoprobe was mechanically manipulated so that it physically deflected the CNF to the right. The CNF sustained bending angles ϕ as large as ϕ ~ 70º (Fig. 5b), and it then returned elastically to its initial position (Fig. 5c). The CNFs were able to tolerate such severe strains over tens of cycles without detachment

from the substrate or fracture within the tube body. These tests show the CNFs are well adhered to the substrate, much like the results of the nanoindentation tests in Fig. 3 indicated, and demonstrate the exceptional elasticity and resilience of PECVD synthesized CNFs for NEMS applications.

3.3 Electrical Actuation in Vertically Oriented Carbon Nanofibers

Two-terminal electrical transport measurements were used to probe the electrical characteristics of individual, as-grown CNFs, formed on refractory metallic nitride buffer layers on Si, as well as those grown directly on degenerately doped Si substrates. Electrostatic switching measurements were also conducted to determine the magnitude of the switching or pull-in voltage V_{pi} and the results were compared to theoretical simulations which are described in more detail in Section 3.4. *In-situ* electrical measurements were conducted on *as grown* CNFs using a nanomanipulator probe stage (Kammrath and Weiss) mounted inside an SEM (FEI Quanta 200F) that was equipped with an electrical feed-through. Tungsten probes were used to make the 2-terminal electrical measurements that were performed with an HP4155C parameter analyzer.

The electrical measurements were performed on CNFs grown directly on degenerately doped Si <100> substrates (resistivity $\rho \sim 1 - 5$ mΩ-cm), as well as refractory NbTiN buffer layers. The NbTiN was ~ 200 nm thick and was deposited using dc magnetron reactive sputtering in a nitrogen ambient on Si substrates. Figure 6a shows a low magnification SEM image of two probes housed on the nanomanipulator stage within the SEM, that were used for the electron transport measurement on individual CNFs. The SEM image in the inset of Fig. 6b shows a nanoprobe that was mechanically manipulated so that it physically contacted an individual CNF grown directly on NbTiN. The other electrode contacted the substrate which served as the ground. From the I-V characteristic in Fig. 6b, we see the CNF was electrically conductive, although measurable currents could not be detected until ~ 6 V, after which point current increased sharply up to ~ 9.5 V. The sub-gap region at low voltages may arise from a native oxide on the tungsten probe tips, which would suppress conductance at low bias voltages. Measurements conducted by Andzane *et al.* have revealed that an oxide layer was responsible for suppressed conductance at low bias voltages for their Ge nanowires.[13]

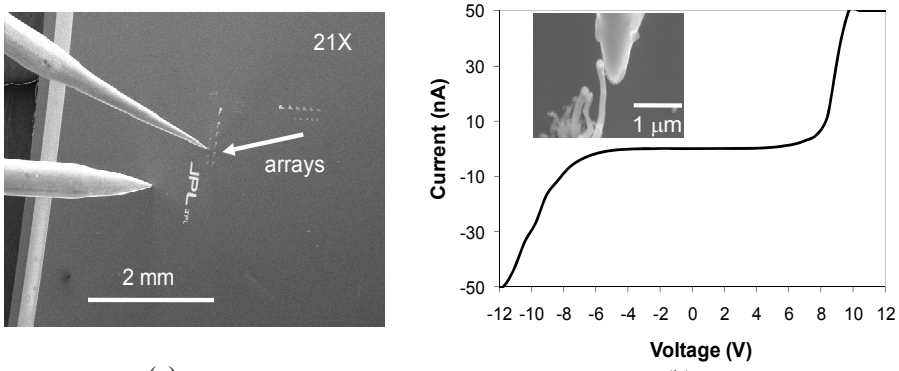

(a) (b)

Figure 6. (a) Low magnification SEM image showing the two probes above the sample that were mechanically manipulated inside the SEM to gather electrical data *in-situ*. b) Electrical transport measurements for a single CNF grown on an NbTiN buffer layer on Si. A nanoprobe was in contact with a CNF, as the SEM image in the inset indicates.

Although it is difficult to ascertain the inherent conductivity of our CNFs from this 2-terminal measurement, prior 4-point measurements performed on individual CNFs that were placed horizontally on oxidized substrates, revealed an inherent CNF resistivity of ~ 4.2 x 10^{-3} Ω-cm.[25] It is not surprising that the CNF resistivity lies well-above that of graphite parallel to the basal plane (4 x 10^{-5} Ω-cm), since electron

transport is likely to occur via inter-plane hopping due to the herring-bone structure in CNFs, as our TEM from Fig. 3 confirmed.

We now examine the electron transport through tubes grown directly on Si, and compare the results to those synthesized directly on NbTiN buffer layers (Fig. 7). Curve (1) in Fig. 7 indicated high conductivity as expected, since both probes were shorted to the substrate. When a CNF grown on NbTiN was probed (curve (2)), a response similar to that shown in Fig. 6b was detected. However, when a CNF grown directly on Si was contacted, no measurable currents could be detected, as indicated by curve (3). Energy-Dispersive-X-ray (EDX) analysis performed by Melechko *et al.*, has indicated the presence of a sheath of SiNx on the CNF sidewalls for tubes synthesized on Si.[26] The presence of such a dielectric coating on the sidewalls of the CNFs grown on Si would explain the data we obtained in curve 3 of Fig. 7. The directional nature of ion bombardment during dc PECVD causes Si from the substrate to be resputtered, which possibly coats the sidewalls of the growing CNFs. Due to the nitrogen-rich gaseous environment during growth (~ 80% NH_3), the Si on the CNF sidewalls reacts with N, potentially resulting in the formation of SiNx. However, any SiNx that forms on the substrate is likely to be removed due to the constant flux of energetic ions bombarding the substrate directly, which explains the result in curve 1. Since sidewall conduction is of little interest for the field emission applications of such CNFs[27] where electron transport occurs internally within the CNF body, *in-situ* nanomanipulation measurements performed here uniquely suggest that CNFs synthesized directly on Si are unsuitable for low voltage dc NEMS applications.

In addition, electrostatic actuation measurements (described in more detail below) of the tubes grown on Si were unsuccessful even up to 100 V, and suggests that a dielectric barrier such as SiNx may also have existed at the Si-to-CNF interface. While SiC may also be present at this interface, a Schottky junction would arise in such an event that would allow transport in the forward-bias regime. In the case of tubes on NbTiN, the measurable electrical conductivity (curve 2) suggests any resputtered NbTiN does not create a thick electrically insulating sheath on the tube sidewalls to prevent conduction, although more nitrogen rich phases could form. More work is necessary to elucidate the nature of the junction at the NbTiN-to-CNF interface.

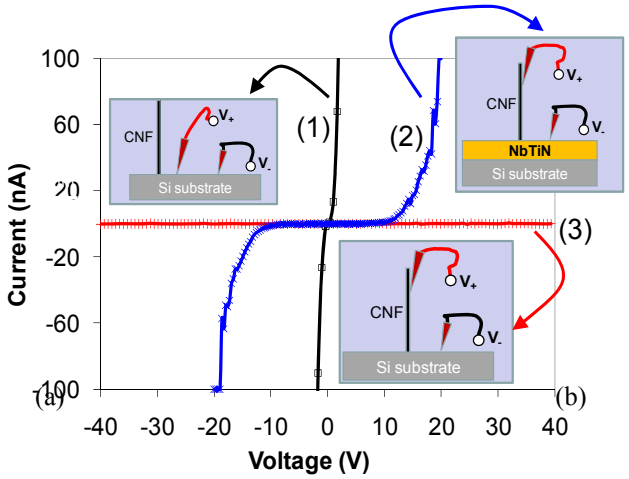

Figure 7. Curve (1) corresponds to the case where both probes were shorted to the substrate and indicates high conductivity; curve (2) shows the CNF grown on NbTiN was electrically conductive; curve (3) corresponds to the case where no electrical conduction was detected for a CNF grown directly on Si, and suggests such CNFs are unsuitable for dc NEMS applications.

Actuation measurements were performed for CNFs on NbTiN, where a nanoprobe was manipulated to within a few hundred nm of a single CNF. The electrostatic force per unit length F_{Elec} increases as $F_{Elec} \prec V^2$,

where V is the voltage, and the elastostatic force per unit length F_{Elasto} increases as $F_{Elasto} \prec EI$, where E and I are the elastic modulus and moment of inertia of the nanotube, respectively.[28] With increasing V ($F_{Elec} > F_{Elasto}$) the tube deflects closer to the probe, and a tunneling current is detected which increases exponentially, and results in a sudden or sharp change in slope at turn-on. In Figure 8a, the SEM image shows a tube just prior to actuation with a tube length $l \sim 2.8$ μm, initial gap $g_0 \sim 160$ nm, tube diameter $d \sim 60$ nm, and a probe-to-tube coupling length $c \sim 0.63$ μm. The SEM image in Fig. 8b shows the tube stuck to the probe after actuation, which is also confirmed by the switching I-V characteristic in Fig. 8c. From Fig. 8c, in the regime where the current rises from a non-zero to a maximal value (between 26 V – 31 V), the data appears to be increasingly noisy which can be attributed to the stochastic nature of the tunneling mechanism. Surface asperities on the W probes may also lead to random fluctuations in the current during the switching process. The SEM image in Fig. 8b suggests that the van der Waals (VDW) force $F_{vdw} > F_{Elasto}$ which is validated by the hysteresis in the I-V of Fig. 8c. While Jang *et al.* also reported stiction for vertically oriented tubes, no hysteresis data was presented that electrically signaled the presence of stiction,[10] as has been reported here.

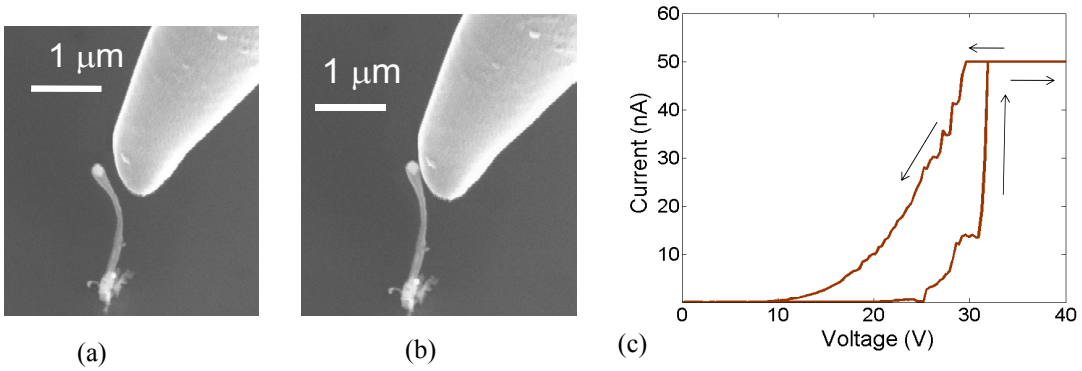

Figure 8. Actuation test where a nanoprobe was within hundred's of nm of a CNF. (a) SEM image for a tube just prior to actuation, with $l \sim 2.8$ μm, $g_0 \sim 160$ nm, $d \sim 60$ nm, and $c \sim 0.63$ μm. (b) SEM image depicting the tube stuck to the probe after actuation. (c) The I-V characteristic for switching showed $V_{pi} \sim 31$ V. Hysteresis in the I-Vs suggests such structures are promising for nonvolatile memory applications.

The SEM image in Fig. 9a shows the same tube but with larger $g_0 \sim 220$ nm just before actuation, while the SEM image in Fig. 9b shows the tube just after actuation. A larger g_0 should increase V_{pi}, which was seen in the I-V of Fig. 9c, where the onset of a current occurs at ~ 32 V (cycle 1). Although the SEM image in Fig. 9b shows the tube stuck to the probe after actuation, with a contact length < 50 nm, it detached prior to the onset of cycle 2. In cycle 2, $V_{pi} \sim 35$ V, but the turn-off was almost identical to cycle 1, since it was dominated by the contact resistance. By increasing the probe-to-tube coupling area and reducing the initial gap, we have observed lower V_{pi} (~ 14 V) as reported elsewhere.[29] In general, this work demonstrates the flexibility of the nanomanipulator to enable the exploration of a wide range of probe-to-tube geometries with ease, without resorting to long design or fabrication cycles. Our measurements suggest such bottom-up synthesized structures are promising for 3D NEMS, in particular for nonvolatile memory applications.

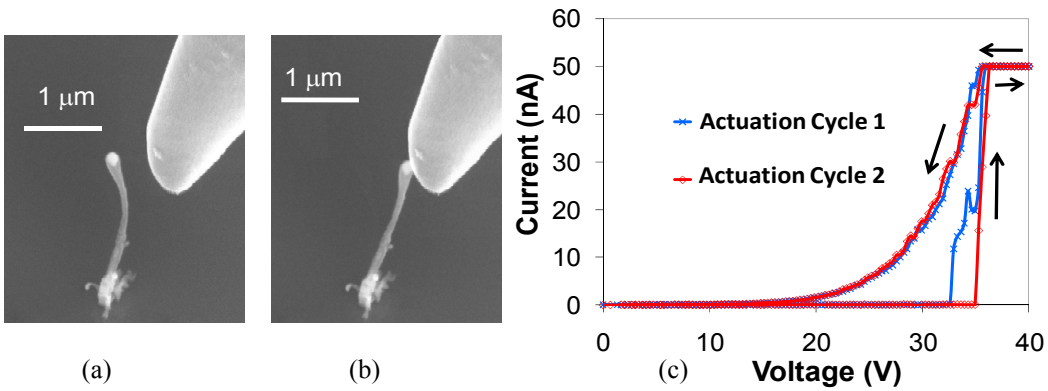

(a) (b) (c)

Figure 9. (a) An SEM image which shows $g_0 \sim 220$ nm for the same CNF in Fig. 8 just before actuation. (b) The SEM image shows the tube after actuation, where it was momentarily stuck to the probe, but detached prior to the onset of cycle 2. (c) The I-V shows 2 switching cycles with turn-on varying slightly (~ 32 V and 35 V) but very little variation was seen in the turn-off cycles which is dominated by the contact resistance.

3.4 Finite-Element-Modeling of Switching Voltage

We have also theoretically calculated the switching voltage and compared the results to those obtained from experiment. The V_{pi}*(analytical)* was calculated using $V_{PI}(analytical) = \sqrt{\frac{8kg_0^3}{27\varepsilon_o wl}}$ where ε_o is the effective permittivity, and w is the beam width (or tube diameter). The spring constant k for a cantilever beam (our tubes are akin to a vertical cantilever) is given by $k = \frac{8EI}{l^3}$. A V_{pi}*(analytical)* ~ 13 V was computed for the geometry in Fig. 8, which assumed the probe and tube couple over l entirely. FEM with COMSOL Multiphysics[30] was used to determine V_{pi}*(numerical),* since the probe interacts with the tube predominately near the tip, as shown by the model geometry in Fig. 10. The V_{pi}*(numerical)* ~ 23 V > V_{pi}*(analytical)* ~ 13 V confirming expectations, since COMSOL accounts for the smaller coupling area between the probe and the tube. The F_{Elec} and F_{Elasto} were calculated by numerically solving the Poisson's equation and the strain tensor, respectively, to determine the equilibrium position of the tube by a force balance analysis. Since electrostatic actuation is a positive feedback effect, an instability arises at a critical gap g_c where no equilibrium solution exists, and the tube collapses to the probe at this pull-in point. In the tube deflection-voltage characteristic of Fig. 10b $\left.\frac{\partial x}{\partial V}\right|_{V=V_{pi}} \to \infty$ occurs at $x = g_c \sim 61$ nm, and V_{pi}*(numerical)* ~ 23 V. With $g_0 \sim 160$ nm, $g_c/g_o = 61$ nm/160 nm ~ 0.38, which is in close agreement with the value obtained in MEM switches ($g_c \sim g_0/3$), as well as continuum simulations on other CNT structures,[28] where $g_c/g_o \sim 0.4$ (e.g. Fig. 10 of Ref. 28). The V_{pi}*(experiment)* was ~ 31 V (Fig. 8c) which did not appear to differ appreciably from the theoretically calculated value. In the near future, we will report on our work in forming and characterizing 3D NEMS switches which comprise of monolithically integrated electrodes in close proximity to individual CNFs.

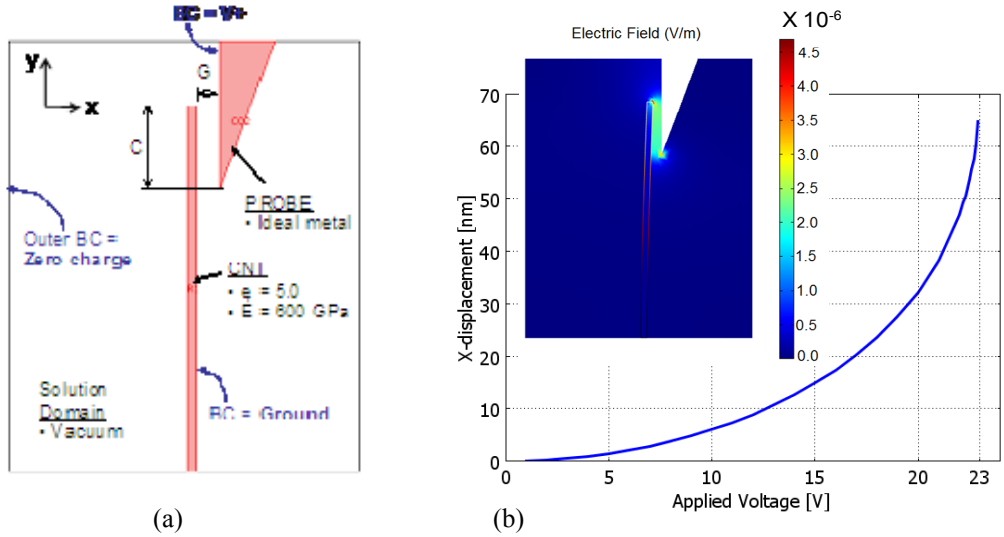

Figure 10. (a) Geometry and boundary conditions used in the FEM simulations. (b) The nanotube tip displacement x as a function of V, E = 600 GPa, l = 2.8 μm, g_0 = 160 nm, d = 60 nm, c = 630 nm (parameters from Fig. 8). Inset showed the spatial profile of the electric field strength at ~ 22.9 V, just prior to pull-in, and indicates the field is distributed between the nanoprobe and CNF. The V_{pi}*(numerical)* ~ 23 V and V_{pi}*(experiment)* ~ 31 V for this geometry.

ACKNOWLEDGMENTS

We sincerely acknowledge Robert Kowalczyk for his assistance with the PECVD growth chamber and performing chamber upgrades as necessary, in addition to Dr. Choonsup Lee, Dr. Richard L. Baron and Dr. Paul von Allmen for useful discussions. We would also like to thank Shelby Hutchens of the California Institute of Technology (Caltech) and Brian Peters of Agilent Technologies for the images taken in Fig. 3a and 3b. We gratefully acknowledge critical support and infrastructure provided for this work by the Kavli Nanoscience Institute at Caltech. This research was carried out at the Jet Propulsion Laboratory, California Institute of Technology, under a contract with the National Aeronautics and Space Administration and was funded through the internal Research and Technology Development (R&TD) program.

REFERENCES

[1] S. Tuukkanen, S. Streiff, P. Chenevier, M. Pinault, H. J. Jeong, S. Enouz-Vedrenne, C. S. Cojocaru, D. Pribat, J. P. Bourgoin, *Appl. Phys. Lett.* **95**, 113108 (2009).
[2] T. Yamada, T. Saito, D. Fabris, C. Y. Yang, *IEEE Elect. Dev. Lett.* **30**, 469 (2009).
[3] International Technology Roadmap for Semiconductors; http://www.itrs.net/reports.html, 2007 Edition.
[4] H. T. Ng, J. Li, M. K. Smith, P. Nguyen, A. Cassel, J. Han, M. Meyyappan, *Science* **300**, 1249 (2003).
[5] P. Kim, C. M. Lieber, *Science* **286**, 2148-2150 (1999).
[6] T. Rueckes, K. Kim, E. Joselevich, G. Y. Tseng, C. L. Cheung, C. M. Lieber, *Science* **289**, 94 (2000).
[7] E. Dujardin, V. Derycke, M. F. Goffman M. F., *Appl. Phys. Lett.* **87**, 193107 (2005).
[8] Z. Chen, L. Tong, Z. Wu, Z. Liu, *Appl. Phys. Lett.* **92**, 103116 (2008).
[9] A. Eriksson, S. Lee, A. A. Sourab, A. Isacsson, R. Kaunisto, J. M. Kinaret, E. E. B. Campbell, *Nano Lett.* **8**, 1224 (2008).

[10] J. E. Jang, S. N. Cha, Y. Choi, G. A. J. Amaratunga, D. J. Kang, D. G. Hasko, J. E. Jung, J. M. Kim, *Appl. Phys. Lett.* **87**, 163114 (2005).
[11] J. E. Jang, S. N. Cha, Y. J. Choi, D. J. Kang, T. P. Butler, D. G. Hasko, J. E. Jung, J. M. Kim, G. A. J. Amaratunga, *Nat. Nanotechnol.* **3**, 26 (2008).
[12] Y. Hayamizu, T. Yamada, K. Mizuno, R. C. Davis, D. N. Futaba, M. Yumura, K. Hata, *Nat. Nanotechnol.* **3**, 289 (2008).
[13] J. Andzane, N. Petkov, A. I. Livshits, J. J. Boland, J. D. Holmes, D. Erts, *Nano Lett.* **9**, 1824 (2009).
[14] C. Ke, H. D. Espinosa, *Small* **2**, 1484 (2006).
[15] A. B. Kaul, E. W. Wong, L. Epp, and B. D. Hunt, *Nano Lett*. **6**, 942 (2006)
[16] D. Peroulis, S. P. Pacheco, K. Sarabandi, L. P. B. Katehi, IEEE Trans. on Microwave Theory and Tech. **51**, 259 (2003).
[17] S. W. Lee, D. S. Lee, R. E. Morjan, S. H. Jhang, M. Sveningsson, O. A. Nerushev, Y. W. Park, and E. E. B. Campbell, Nano. Lett. **4**, 2027 (2004).
[18] S. Brinkmann, Y-J. Kim Y-J, J. R. Greer, *Phys. Rev. Lett.* **100**, 155502 (2008).
[19] Y. Ominami, Q. Ngo, A J. Austin, H. Yoong, C. Y. Yang, A. M. Cassell, B. A. Cruden, J. Li, M. Meyyappan, *Appl. Phys. Lett.* **87**, 233105 (2005).
[20] J. F. Waters, L. Riester, M. Jouzi, P. R. Guduru, J. M. Xu, *Appl. Phys. Lett.* **85**, 1787 (2004).
[21] H. J. Qi, K. B. K. Teo, K. K. S. Lau, M. C. Boyce, W. I. Milne, J. Robertson, K. K. Gleason, *J. of the Mech. and Phys. of Solids* **51**, 2213 (2003).
[22] Y. Hayamizu, R. C. Davis, T. Yamada, D. N. Futaba, S. Yasuda, M. Yumura, K. Hata, *Phys. Rev. Lett.* **102**, 175505 (2009).
[23] B. I. Yakobson, C. J. Brabec, J. Bernholc, *Phys. Rev. Lett*. **76**, 2511 (1996).
[24] T. Fukuda, F. Arai, L. Dong, *Proc. IEEE* **91**, 1803 (2003).
[25] L. Zhang, D. Austin, V. Merkulov, A. V. Meleshko, K. L. Klein, M. A. Guillorn, D. H. Lowndes, M. L. Simpson, *Appl. Phys. Lett.* **84**, 3972 (2004).
[26] A. V. Melechko, T. E. McKnight, D. K. Hensley, M. A. Guillorn, A. Y. Borisevich, V. I. Merkulov, D. H. Lowndes, M. L. Simpson, *Nanotech.* **14**, 1029 (2003).
[27] N. Shimoi, S. Tanaka, *Carbon* **47**, 1258 (2009).
[28] M. Dequesnes, S. V. Rotkin, and N. R. Aluru, *Nanotech.* **13**, 120 (2002).
[29] A. B. Kaul, A. Khan, L. Bagge, K. G. Megerian, H. G. LeDuc, and L. Epp, *Appl. Phys. Lett.* **95**, 093103, (2009).
[30] COMSOL Multiphysics Version 3.4, COMSOL AB, Tegnérgatan 23, SE-111 40, Stockholm, Sweden. www.comsol.com.